Large-Signal Equivalent Circuit for Datacom VCSELs – Including Intensity Noise

Citation for the original published paper (version of record):
Grabowski, A., Gustavsson, J., Larsson, A. (2022). Large-Signal Equivalent Circuit for Datacom VCSELs – Including Intensity Noise. Journal of Lightwave Technology: 1-9.
http://dx.doi.org/10.1109/JLT.2022.3200905

Large-Signal Equivalent Circuit for Datacom VCSELs – Including Intensity Noise

Alexander Grabowski, *Student Member, IEEE*, Johan S. Gustavsson, and Anders Larsson, *Fellow, IEEE*

***Abstract*— Optical interconnects (OIs) continue to require more and more sophisticated driver and receiver electronics as higher baud rates are pushed in datacom, mainly due to the bandwidth stagnation of the optoelectronic components such as the vertical-cavity surface-emitting laser (VCSEL) in the transmitter as well as the photodetector (PD) in the receiver. Another important focus is maintaining high energy efficiency for the OIs. For both cases, a reliable equivalent circuit model for high-speed VCSELs is required for link optimization. This work is an extension of our previously presented large-signal VCSEL equivalent circuit model, where noise is added to the physical processes that the VCSEL model is based on. Thus, a new step is taken in the strive of developing an even more accurate physics-based large-signal VCSEL equivalent circuit model for datacom applications. Following a detailed description of the VCSEL noise modelling, a presentation is given on simulated results of VCSEL relative intensity noise (RIN) spectrum and eye diagrams under 28 Gbaud on-off keying (OOK) and pulse-amplitude 4 (PAM4) modulation, and that are compared with corresponding measurement results. Good agreement is found over a wide range of VCSEL driving conditions and temperatures. A 28-GHz-bandwidth VCSEL is applied for the demonstration, and the presented noise extended VCSEL equivalent circuit model was implemented in Verilog-A, and the simulations were performed using Cadence Spectre.**

***Index Terms*— Data communication, equivalent circuits, semiconductor device modeling, semiconductor lasers, semiconductor device noise, white noise.**

I. Introduction

As the datacom industry expands due to higher customer demands, higher baud rates and more energy efficient electronics are paramount in optical interconnects (OIs). The OIs mainly consist of uncooled GaAs-based vertical-cavity surface-emitting lasers (VCSELs), multimode optical fibers (MMFs) and pin-photodetectors (PDs) as this is the most energy- and cost effective solution [1]. However, due to physical bandwidth constraints of the optoelectronics such as the VCSEL and the PD at around 30 GHz, co-optimization with transceiver electronics is paramount for next-gen OIs to meet future datacom standards and keep the links energy efficient. For these types of links, the VCSEL intensity noise is typically the dominant noise [2], and especially impactful for multi-level modulation formats.

Therefore, our comprehensive physics-based large-signal equivalent circuit model for datacom VCSELs, previously presented in [3], where it was proven to be able to reproduce the large-signal output waveforms over a broad range of bias currents, ambient temperatures and modulation formats, is in this work extended to also include the intensity noise properties in the VCSEL output. A detailed theoretical description of the noise implementation is here provided, which is based on that each internal physical process of carrier transport and recombination, and photon generation and loss etc., is noisy by nature. The noise extended model is thereafter demonstrated via comparison of simulated to measured VCSEL relative intensity noise (RIN) spectra and also large signal on-off keying (OOK) and pulse-amplitude 4 (PAM4) eye diagrams of a simple back-to-back link set-up. The comparison is done for a wide range of bias currents, modulation voltages and ambient temperatures.

To our knowledge, there are no published large-signal VCSEL equivalent circuit models with such comprehensive "per-process" noise implementations, and that have been demonstrated to work over a broad range of bias currents, ambient temperatures and modulation formats. The authors believe this "per-process" noise treatment is necessary to be able to accurately predict the frequency-dependent VCSEL noise properties over a broad range of VCSEL driving conditions. Most of the similar works, such as of [4] and [5], adopt simpler noise modelling, i.e. not "per-process" noise implementations, but instead introduce different types of approximations, for example to consider that the spontaneous emission coupled into the lasing optical field being the dominant noise source and only including it. While this is not a wrong assumption, the authors believe that our implementation is physically more accurate and thus provides better agreement to measurements of VCSEL output. The works of [4] and [5] have also not demonstrated their model's validity over a broad range of bias currents, ambient temperatures and modulation formats as we have done in this work.

Our noise modelling mainly follows the noise theory presented in [6], which is based on the temporal uncertainty,

Manuscript received May 7, 2022. This work was supported by the Swedish Foundation for Strategic Research (SSF). (Corresponding author: Alexander Grabowski.)

Alexander Grabowski, Johan Gustavsson, and Anders Larsson are with the Photonics Laboratory, Department of Microtechnology and Nanoscience (MC2), Chalmers University of Technology, SE-41296 Gothenburg, Sweden (email: alexander.grabowski@chalmers.se; johan.gustavsson@chalmers.se; anders.larsson@chalmers.se).

following Poisson statistics, for the various physical processes taking place inside the VCSEL. This in particular in the separate confinement heterostructure (SCH) where carriers are transported, trapped, annihilated, or escaped via carrier diffusion, recombination, leakage etc., and photons are generated and absorbed via stimulated and spontaneous emission and stimulated absorption.

This paper is organized as follows. In Section II the noise extension in our established large-signal VCSEL equivalent circuit model [3] is presented in detail, and in Section III this updated circuit model is demonstrated, applying the same VCSEL as in [3]. Simulations of VCSEL RIN spectra are first compared to measurements. Thereafter, simulations of eye diagrams of a simple back-to-back VCSEL link, operating at 28 Gbaud OOK and PAM4 modulation, are compared to measurements. Finally, conclusions are given in Section IV.

II. VCSEL Noise Equivalent Circuit

The starting point of this work is the large-signal equivalent circuit model for datacom VCSELs that was previously developed by the authors and presented in detail in [3], and that can well reproduce the optical output waveform generated by a high-speed 850-nm VCSEL under different modulation conditions. This large-signal equivalent circuit, which consists of five interdependent sub-circuits, is here extended so that it can also reproduce the intensity noise properties in the output from the same VCSEL. This is done by adding several noise sources to sub-circuits 1 to 4 (as these sub-circuits model physical processes in the VCSEL that are stochastic by nature), which is explained in the following sub-sections, and results in an updated equivalent circuit as illustrated in Fig. 1.

A. Sub-Circuit 1: Input Impedance and Voltage Drop

For sub-circuit 1 in [3], all resistors in the input impedance circuit contribute with Johnson-Nyquist (thermal) noise. This is modelled by adding a current noise source in parallel to each resistor, which produces white noise with a double-sided spectral density, $S_{I_R^{noise}}$ [A^2/Hz] given by [7]:

$$S_{I_R^{noise}}(R) = \frac{2 \cdot k \cdot T}{R}, \tag{1}$$

where k is Boltzmann's constant, T [K] is the temperature, and R [Ω] is the resistance of the resistor. Note that T is the internal VCSEL temperature (traced by sub-circuit 5 [3]) and not the ambient temperature. In addition, to be able to account for a noisy VCSEL driver (current source) a current noise source is added in parallel to the voltage source U_{SCH} [V] that represents the voltage drop over the SCH. This current noise source is expressed as a shot noise source [8] having a double-sided spectral density, $S_{I_{SCH}^{noise}}$ [A^2/Hz] given by

$$S_{I_{SCH}^{noise}}(I_{SCH}) = \eta_{shot} \cdot q \cdot I_{SCH}, \tag{2}$$

where q is the elementary charge and I_{SCH} [A] is the current reaching the SCH. $\eta_{shot} \geq 0$ is a factor to model the noise level (in relation to the shot noise level) of the VCSEL driver, where $\eta_{shot} = 0$ and $\eta_{shot} = 1$ correspond to a driver that is noise free or has full shot noise, respectively. η_{shot} can of course be much greater than one for a noisy driver. In this description, the driver noise is assumed to be pure white noise, and pink noise ($1/f$ flicker noise) is thus neglected. This is motivated by that these VCSELs will be operated at modulation frequencies that are far beyond the corner frequency for flicker noise, and also that the VCSEL phase noise is not of concern for the targeted application.

Finally, note that apart from the above-mentioned thermal and shot noise sources, U_{SCH} will in itself be noisy as a result of the stochastic carrier capture, carrier recombination, and thermionic emission processes in the SCH and quantum wells (QWs), as outlined in Section II-B below. Strictly, this will contribute to noise in I_{SCH} if the VCSEL driver is voltage driven, but not if it is current driven.

B. Sub-Circuit 2 and 3: Charge Accumulation in SCH

For the SCH, the rate equation (8) in [3] that is used to describe the change in carriers accumulated in the continuum, n_B [-], with time, t [s], is added with noise terms for the spontaneous carrier recombination, QW carrier capture, QW carrier escape, and SCH carrier leakage processes as they are by nature stochastic:

$$\frac{dn_B}{dt} = i_{inj} - i_{sp,B} - i_{cap} + i_{esc} - i_{leak} - i_{sp,B}^{noise}(t) - i_{cap}^{noise}(t) + i_{esc}^{noise}(t) - i_{leak}^{noise}(t), \tag{3}$$

where $i_{sp,B}^{noise}$, i_{cap}^{noise}, i_{esc}^{noise} and i_{leak}^{noise} are four Langevin noise sources that model the fluctuations in the spontaneous carrier recombination rate, QW carrier capture rate, QW carrier escape rate, and SCH carrier leakage rate, respectively. Each of these four stochastic processes are assumed to be a Poisson process [6], which produces shot noise, i.e. white noise, with a double-sided spectral density related to the average rate of the process. This means that $i_{sp,B}$, i_{cap}, i_{esc}, and i_{leak}, now represent the average rates for the spontaneous carrier recombination, QW carrier capture, QW carrier escape, and SCH carrier leakage processes, respectively, and that the double-sided spectral density for the noise in the spontaneous carrier recombination rate $S_{i_{sp,B}^{noise}}$ [1/s^{2}Hz], QW carrier capture rate $S_{i_{cap}^{noise}}$ [1/s^{2}Hz], QW carrier escape rate $S_{i_{esc}^{noise}}$ [1/s^{2}Hz], and SCH carrier leakage rate $S_{i_{leak}^{noise}}$ [1/s^{2}Hz], are

$$S_{i_{sp,B}^{noise}} = i_{sp,B}, \quad S_{i_{cap}^{noise}} = i_{cap}, \quad S_{i_{esc}^{noise}} = i_{esc}, \quad S_{i_{leak}^{noise}} = i_{leak}. \tag{4}$$

Thus, to sub-circuit 2 in [3], which is the rate equation for n_B translated into an equivalent circuit, four corresponding current noise sources are added in parallel to the respective current sources describing the average rates, and having zero mean and the following double-sided spectral densities with unit in [A^2/Hz]

$$S_{I_{sp,B}^{noise}} = q \cdot I_{sp,B}, \quad S_{I_{cap}^{noise}} = q \cdot I_{cap}, \quad S_{I_{esc}^{noise}} = q \cdot I_{esc}, \quad S_{I_{leak}^{noise}} = q \cdot I_{leak}. \tag{5}$$

This article has been accepted for publication in IEEE/OSA Journal of Lightwave Technology. This is the author's version which has not been fully edited and content may change prior to final publication. Citation information: DOI 10.1109/JLT.2022.3200905

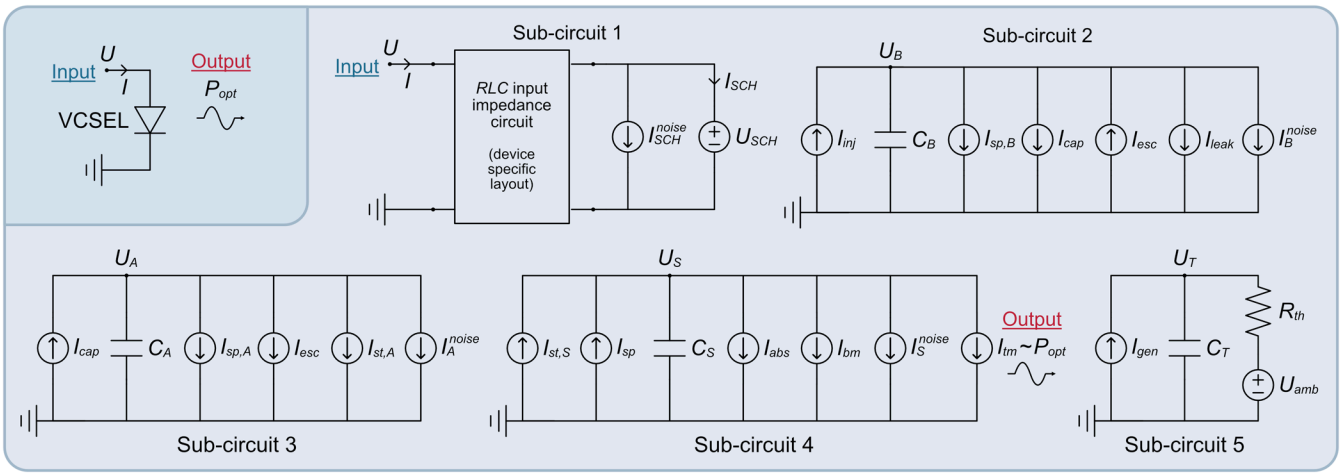

Fig. 1. Equivalent circuit for a high-speed datacom VCSEL, with noise sources included.

The rate equation (9) in [3] that is used to describe the change in carriers accumulated in the QWs, n_A [-], with time, is similarly added with noise terms. Noise terms for the spontaneous and stimulated carrier recombination, and stimulated absorption processes are included as they are also by nature stochastic,

$$\frac{dn_A}{dt} = i_{cap} - i_{sp,A} - i_{esc} - i_{st} + i_{cap}^{noise}(t) - i_{sp,A}^{noise}(t) - i_{esc}^{noise}(t) - i_{st.rec}^{noise}(t) + i_{st.abs}^{noise}(t). \quad (6)$$

Since n_A and n_B are interlinked via the QW carrier capture and QW carrier escape processes, (6) has the same two Langevin noise sources i_{cap}^{noise} and i_{esc}^{noise} as in (3). Note that the noise sources are added with different sign in (6) compared to in (3) due to the anti-correlation, i.e. that the loss of one carrier in n_B results in the gain of one carrier in n_A.

Furthermore, $i_{sp,A}^{noise}$, $i_{st.rec}^{noise}$ and $i_{st.abs}^{noise}$ are Langevin noise sources that model the fluctuation in the spontaneous and stimulated carrier recombination rate, and stimulated absorption rate, respectively. Each of these three stochastic processes are also assumed to follow Poisson statistics, and where it is recognized that i_{st} symbolizes the net average rate of the stimulated recombination and absorption processes, i.e.

$$i_{st} = i_{st.rec} - i_{st.abs}, \quad (7)$$

where

$$i_{st.rec} = \eta_{sp} \cdot i_{st}, \quad i_{st.abs} = (\eta_{sp} - 1) \cdot i_{st}. \quad (8)$$

η_{sp} [-] is the population inversion factor and is related to the quasi-Fermi-level separation and the two energy levels involved for the lasing [9]. For simplicity it is approximated by [10],

$$\eta_{sp} \approx \frac{n_A}{(n_A - n_{tr})}, \quad (9)$$

where n_{tr} [-] is the number of accumulated free carriers in the QWs needed to reach optical transparency, and indirectly computed from:

$$g(n_A = n_{tr}, S = 0, T) = 0, \quad (10)$$

where g is the optical material gain in the QWs, modelled by the function (17) in [3], and S [-] is the number of photons in the optical resonator.

This gives that the double-sided spectral density for the noise in the spontaneous carrier recombination rate, $S_{i_{sp,A}^{noise}}$ [1/s^{2}Hz], stimulated carrier recombination rate, $S_{i_{st.rec}^{noise}}$ [1/s^{2}Hz], and stimulated absorption rate, $S_{i_{st.abs}^{noise}}$ [1/s^{2}Hz], is

$$S_{i_{sp,A}^{noise}} = i_{sp,A}, \quad S_{i_{st.rec}^{noise}} = \eta_{sp} \cdot i_{st}, \quad S_{i_{st.abs}^{noise}} = (\eta_{sp} - 1) \cdot i_{st}. \quad (11)$$

Thus, to sub-circuits 3 in [3], which is the rate equation for n_A translated into an equivalent circuit, five corresponding current noise sources are added in parallel to the respective current sources describing the average rates, where two of the current noise sources are the same as the ones used in sub-circuit 2 with double-sided spectral densities as defined in (5). The other three current noise sources have zero mean and the following double-sided spectral densities in unit [A^2/Hz]

$$S_{I_{sp,A}^{noise}} = q \cdot I_{sp,A}, \quad S_{I_{st.rec,A}^{noise}} = q \cdot \eta_{sp} \cdot I_{st,A}, \quad S_{I_{st.abs,A}^{noise}} = q \cdot (\eta_{sp} - 1) \cdot I_{st,A}. \quad (12)$$

C. Sub-Circuit 4: Photon Accumulation in Resonator

The rate equation (27) in [3] that is used to describe the change in photons accumulated in the resonator, S [-], with time, is similarly added with noise terms. Noise terms for the loss rates of photons through free-carrier absorption in the doped distributed Bragg reflectors (DBRs), and through the bottom and top DBR are included as they are also by nature stochastic:

$$\frac{dS}{dt} = i_{st} + i_{sp} - i_{abs} - i_{bm} - i_{tm} + i_{st,rec}^{noise}(t) - i_{st,abs}^{noise}(t) - i_{abs}^{noise}(t) - i_{bm}^{noise}(t) - i_{tm}^{noise}(t). \quad (13)$$

Since S and n_A are interlinked via the stimulated carrier recombination and stimulated absorption processes, (13) has the same two Langevin noise sources $i_{st.rec}^{noise}$ and $i_{st.abs}^{noise}$ as in (6). Note that they are added with different sign in (13) compared to in (6) due to the anti-correlation, i.e. that the loss of one carrier in n_A results in the gain of one photon in S. i_{abs}^{noise}, i_{bm}^{noise} and i_{tm}^{noise} are Langevin noise sources that model the fluctuation in the photon loss rate through free-carrier absorption in the DBRs, and through bottom and top DBRs, respectively. Each of these three stochastic processes are also assumed to be a Poisson process [6]. The spontaneously emitted photons in the QWs that contribute to the number of photons in the lasing mode, is also a stochastic process following Poisson statistics, however the average rate, i_{sp}, is much lower than the average rates for stimulated carrier recombination, $i_{st,rec}$, near and above threshold, wherefore its noise contribution is neglected. Note, however, that with the introduction of η_{sp} in (8), i_{sp} can via Einstein's coefficients be related to i_{st} [9], [11] instead of computing it as (28) in [3]. This leads to

$$i_{sp}(n_A, S, T) = \eta_{sp}(n_A, T) \cdot \Gamma \cdot v_g \cdot g(n_A, S, T). \quad (14)$$

This yields that the double-sided spectral density for the noise in the photon loss rate through free-carrier absorption in the DBRs, $S_{i_{abs}^{noise}}$ [1/s^{2}Hz], the photon loss rate through bottom DBR, $S_{i_{bm}^{noise}}$ [1/s^{2}Hz], and the photon loss rate through top DBR, $S_{i_{tm}^{noise}}$ [1/s^{2}Hz], is

$$S_{i_{abs}^{noise}} = i_{abs}, \quad S_{i_{bm}^{noise}} = i_{bm}, \quad S_{i_{tm}^{noise}} = i_{tm}. \quad (15)$$

Thus, to sub-circuit 4 in [3], which is the rate equation for S translated into an equivalent circuit, five corresponding current noise sources are added in parallel to the respective current sources describing the average rates, where two of the current noise sources are the same as the ones used in sub-circuit 3, apart from a factor η, where

$$\eta = \frac{hc}{q\lambda}. \quad (16)$$

The five current noise sources have zero mean and the following double-sided spectral densities in unit [A^2/Hz]:

$$S_{I_{st,rec,S}^{noise}} = \eta^2 \cdot S_{I_{st,rec,A}^{noise}}, \quad S_{I_{st,abs,S}^{noise}} = \eta^2 \cdot S_{I_{s\,t,abs,A}^{noise}}, \quad S_{I_{abs}^{noise}} = \eta \cdot q \cdot I_{abs}, \quad S_{I_{bm}^{noise}} = \eta \cdot q \cdot I_{bm}, \quad S_{I_{tm}^{noise}} = \eta \cdot q \cdot I_{tm}. \quad (17)$$

D. Summary

Fig. 1 illustrates the noise-extended VCSEL equivalent circuit model where, for compactness, the current noise sources in sub-circuits 2, 3, and 4 are lumped together into a single respective current noise source I_{B}^{noise}, I_{A}^{noise} and I_{S}^{noise}, where thus

$$I_B^{noise} = -I_{sp,B}^{noise} - I_{cap}^{noise} + I_{esc}^{noise} - I_{leak}^{noise}, \quad (18)$$

$$I_A^{noise} = -I_{sp,A}^{noise} + I_{cap}^{noise} - I_{esc}^{noise} + I_{st,abs,A}^{noise} - I_{st,rec,A}^{noise}, \quad (19)$$

$$I_S^{noise} = -I_{abs}^{noise} - I_{bm}^{noise} - I_{tm}^{noise} - I_{st,abs,S}^{noise} + I_{st.rec,S}^{noise}, \quad (20)$$

Note that Fig. 1 does not illustrate all noise sources included in sub-circuit 1 where, as mentioned above, all distributed resistors are added with thermal noise.

The optical output power from the VCSEL, P_{opt} [W], is proportional to the current, I_{tm}[A], where I_{tm} is defined in Fig. 1. For a constant VCSEL drive current, I, this results in a noisy output power $P_{opt}(I,t)$, having mean value $\langle P_{opt}\rangle(I)$ (equal to $P_{opt}(I)$ in [3]) and a frequency dependent double-sided spectral density $S_{P_{opt}}(I,f)$ [W^2/Hz], where f [Hz] is the noise frequency.

III. Demonstration on a 28-GHz-Bandwidth VCSEL

In this paper our noise expanded VCSEL equivalent circuit model is demonstrated on a state-of-the-art 28-GHz-bandwidth 850-nm VCSEL, which is the identical VCSEL applied to demonstrate our noise-free version of our VCSEL equivalent circuit model presented in [3]. The VCSEL design is described in detail in [12], [13]. Moreover, the detailed physics behind our noise-free VCSEL model and all its relevant parameters can consequently be found in [3]. The parameter values used in this work are the exact same as those tabulated in [3] (and remain unchanged for all simulations). This means that no further VCSEL parameter value fitting/fine-tuning based on our measured VCSEL noise properties presented below has been done. In this work our equivalent circuit model is implemented in Verilog-A, and the simulations have been performed in Cadence Spectre. The reason for the implementation in Verilog-A is that it was found simpler to introduce the noise sources (and their respective correlation properties), especially for large-signal time domain simulations. Simulated and measured VCSEL RIN spectrum are compared for different VCSEL bias currents and ambient temperatures, and likewise large-signal eye diagrams for a simple back-to-back link operating at 28 Gbaud under pseudorandom bit sequence of word length 2^{15}-1 (PRBS 15) OOK and PAM4 modulation, at different VCSEL bias currents, modulation voltages, and ambient temperatures.

A. VCSEL Relative Intensity Noise

The VCSEL RIN in the frequency domain, $RIN(I,f)$ [1/Hz], is defined by

$$RIN(I,f) = \frac{2 \cdot S_{P_{opt}}(I,f)}{\left(\langle P_{opt}\rangle(I)\right)^2}, \quad (21)$$

where $S_{P_{opt}}(I,f)$ is equal to the Fourier transform (**F**) of the auto-correlation of $P_{opt}(I,t)$ in the time domain, i.e.

This article has been accepted for publication in IEEE/OSA Journal of Lightwave Technology. This is the author's version which has not been fully edited and content may change prior to final publication. Citation information: DOI 10.1109/JLT.2022.3200905

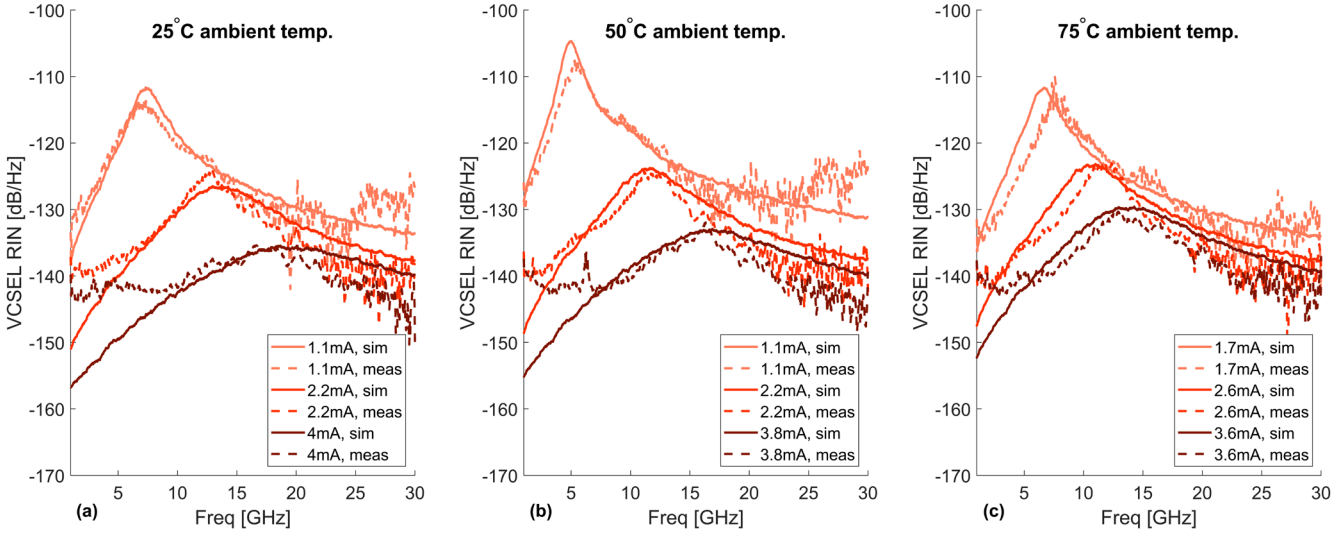

Fig. 2. Measured and simulated RIN spectrum for our 28-GHz-bandwidth VCSEL, for different VCSEL bias currents and ambient temperatures, (a) 25°C, (b) 50°C, and (c) 75°C. Solid lines indicate simulated values while the dashed lines indicate measured values.

$$S_{P_{opt}}(I,f) = \boldsymbol{F}\{\langle P_{opt}(I,t)P_{opt}(I,t-\tau)\rangle\} = \left|\boldsymbol{F}\{P_{opt}(I,t)\}\right|^2. \quad (22)$$

As our noise extended equivalent circuit model is implemented for time domain simulations, the RIN spectrum is thus obtained by tracing $P_{opt}(I,t)$ over a certain time period by applying the equivalent circuit in Fig. 1 for a constant VCSEL drive current I, and thereafter making a Fourier transform of the noisy output power during this period. A temporal resolution of 1 ps or better is used, and with a time period of 1 µs a spectral resolution of 1 MHz is obtained for the simulated RIN spectrum. Furthermore, in these simulations η_{shot} is set to 0.

Experimentally, the VCSEL RIN is measured using an electrical spectrum analyzer (ESA). A current source [Yokogawa 7651] feeds the VCSEL with a DC-current through an RF-probe [Picoprobe 40A]. The VCSEL output beam is passed through an 850-nm-anti-reflection-coated lens package, via first a collimating lens and then a focusing lens to efficiently couple the light into an OM4 MMF that has an FC/APC-type input connector. The latter is used for avoiding optical feedback to the VCSEL. Note that by having a high fiber-coupling efficiency one also avoids mode-partition-noise from mode-selective fiber-coupling that will otherwise contribute to the measured VCSEL RIN spectrum at low frequencies [14].

Moreover, the MMF is short (1 m) to avoid effects from fiber modal dispersion during propagation. The output end of the fiber is via a FC/PC-type connector connected to a PD [New Focus 1481-S-50], which in turn is connected to a microwave amplifier [SHF 806P] that is necessary to boost the signal above the noise floor of the ESA [Agilent Tech. PXA SA N9030A], otherwise most of the spectral components of the VCSEL intensity noise ends up below the noise floor of the ESA. The temperature is controlled using a Peltier element connected to the chuck on which the VCSEL is placed during the experiment.

With all the components connected and the VCSEL turned on, the ESA measures the noise spectrum of the full system, i.e. VCSEL intensity noise, thermal noise from the PD and microwave amplifier, and shot noise from the PD. Thus, the latter two noise contributions need to be determined and subtracted from the measured system noise spectrum in order to deduce the VCSEL RIN spectrum. The thermal noise from the PD and microwave amplifier is determined by measuring the system noise with the ESA when the VCSEL is turned off. The shot noise from the PD is calculated based on the photocurrent generated in the PD. When deducing the VCSEL RIN the bandwidth-limited modulation response of both the PD and the microwave amplifier (supplied by the manufacturer) is also compensated for. Results from RIN simulations and measurements can be seen in Fig. 2, which shows the RIN for our 28-GHz-bandwidth VCSEL at ambient temperatures of 25°C, 50°C and 75°C, for various bias currents specified in the legends. Measuring VCSEL RIN spectrum is challenging, particularly at high bias currents, as the measured spectral noise power levels are close to or go below the noise floor of the ESA, and also that the measurements are highly sensitive to mode-selective fiber-coupling and optical feedback effects. Considering this, a good conformity is found between the measured and simulated VCSEL RIN data, especially around the peak maximum (which corresponds to the VCSEL resonance frequency) in terms of absolute value and spectral distribution. Even though a lot of effort was made on optimizing the measurement set-up one can still see in the measured RIN data in Fig. 2 that there is some small mode-partition noise contribution from mode-selective fiber-coupling, appearing at the very lowest frequencies at high bias currents. One can also observe that there are some minor peaks for frequencies beyond the VCSEL resonance frequency that results from some optical feedback effects. Moreover, the good correlation between the magnitudes of the simulated and measured RIN spectra makes our initial assumption of setting $\eta_{shot} = 0$, reasonable. In other words, the noise in the driver current is relatively low and has little influence on the RIN.

This article has been accepted for publication in IEEE/OSA Journal of Lightwave Technology. This is the author's version which has not been fully edited and content may change prior to final publication. Citation information: DOI 10.1109/JLT.2022.3200905

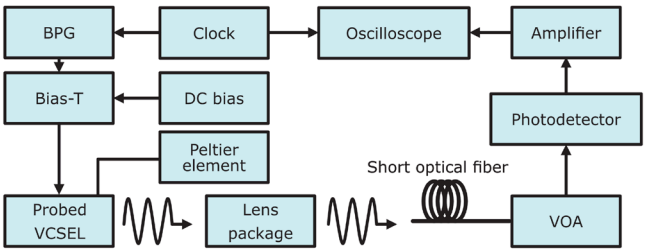

Fig. 3. A block diagram illustrating the experimental setup used in the large-signal performance measurements.

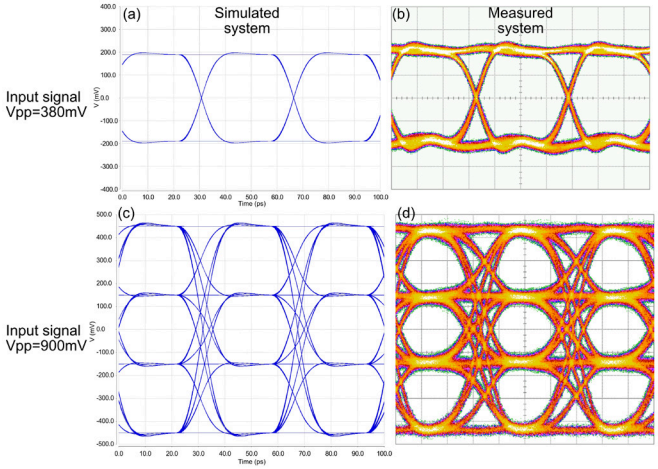

Fig. 4. Input electrical eye diagrams at 28 Gbaud with an ideal 50 Ω load: (a) simulated, OOK-modulation; (b) measured, OOK-modulation; (c) simulated, PAM4-modulation; and (d) measured, PAM4-modulation.

B. Large-signal performance

The experimental link is set up by placing the VCSEL chip on a temperature-controlled metal chuck, and a bias-T is used to combine the data signal with the VCSEL bias current, and this is fed to the VCSEL using an RF-probe [Picoprobe 40A]. The data signal is composed of a PRBS 15 sequence and is generated by a bit pattern generator (BPG) [SHF 12103B]. The bias current is generated by a programmable current source [Yokogawa 7651]. The OOK pattern is generated directly from one port of the BPG, and the PAM4 pattern is generated by combining the output from two separate output ports of the BPG and using a power combiner and delaying one of the bit patterns. The same double-lens package and OM4 MMF set-up as for the RIN-measurements is used to couple the VCSEL output beam to the fiber with high efficiency and propagating the light to the PD, but in this case via a fiber-coupled variable optical attenuator (VOA) [EXFO FVA-3150] that is needed to not exceed the optical power limit of the PD. The 32.3 GHz bandwidth PD [Thorlabs DXM30BF] has a DC-current monitoring port (with output proportional to the DC-photocurrent generated in the PD), and the RF-output of the PD is connected to a 55 GHz bandwidth microwave amplifier [SHF 804TL]. The amplifier output signal is analyzed using a 70 GHz bandwidth equivalent time oscilloscope [Agilent Infiniium DCA-J 86100C]. A block diagram of this setup can be seen in Fig. 3.

The simulations have been run in the Cadence Spectre simulator. In our simulations, to as closely as possible mirror the experimental link set-up, a simple equivalent circuit for the VCSEL driver stage is implemented in Cadence Virtuoso. This driver stage consists of a DC current source and a vsource voltage source (from analogLib) that are combined via an "ideal" bias-T. The vsource voltage source is set to generate an "ideal" 28 Gbaud PRBS 15 OOK (or PAM4) signal with on and off voltage levels that correspond to what is used in the measurements. To capture the correct rise- and fall-time characteristics, as well as the edge smoothness of the digital signal, in the signal driving the VCSEL (determined from a separate measurement, see [3]) the signal is further low-pass filtered using a 50 GHz bandwidth 2-order Butterworth filter. Also, in these simulations η_{shot} is set to 0. To show the simulated driving signal and how it correlates with the measured one, Fig. 4 displays the noise free simulated and measured 28 Gbaud OOK and PAM4 eye diagrams for an ideal 50 Ω load (instead of the VCSEL) and with a peak-to-peak modulation voltage, V_{pp}, of 380 and 900 mV, respectively.

Similarly, a simple equivalent circuit for the receiver stage is implemented in Cadence Virtuoso. This receiver stage consists of first a voltage-controlled voltage-source to mimic the VOA in dampening the received optical signal amplitude before the PD. Secondly, a simple PD equivalent circuit, which provides the same responsivity and frequency response as our PD, and that also adds its thermal and shot noise characteristics. The former magnitude is based on the PD specifications from the manufacturer, while the latter magnitude is computed and being

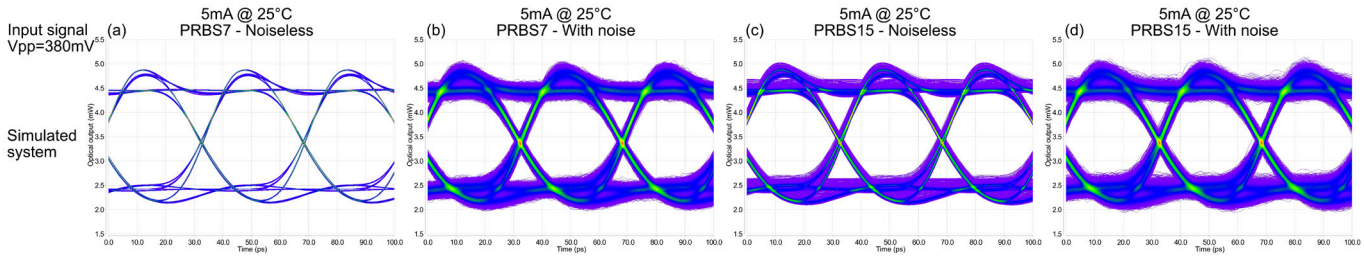

Fig. 5. Simulated eye diagrams at 28 Gbaud OOK modulation for the 28-GHz bandwidth VCSEL and driver alone (i.e. not for the complete back-to-back link set-up) while operating at 25°C with a 5 mA VCSEL bias current and a 380 mV peak-to-peak driver signal amplitude. (a) PRBS 7 word length, all VCSEL noise sources disabled, (b) PRBS 7 word length, all VCSEL noise sources enabled, (c) PRBS 15 word length, all VCSEL noise sources disabled, and (d) PRBS 15 word length, all VCSEL noise sources enabled. The eye diagrams are presented in density function mode.

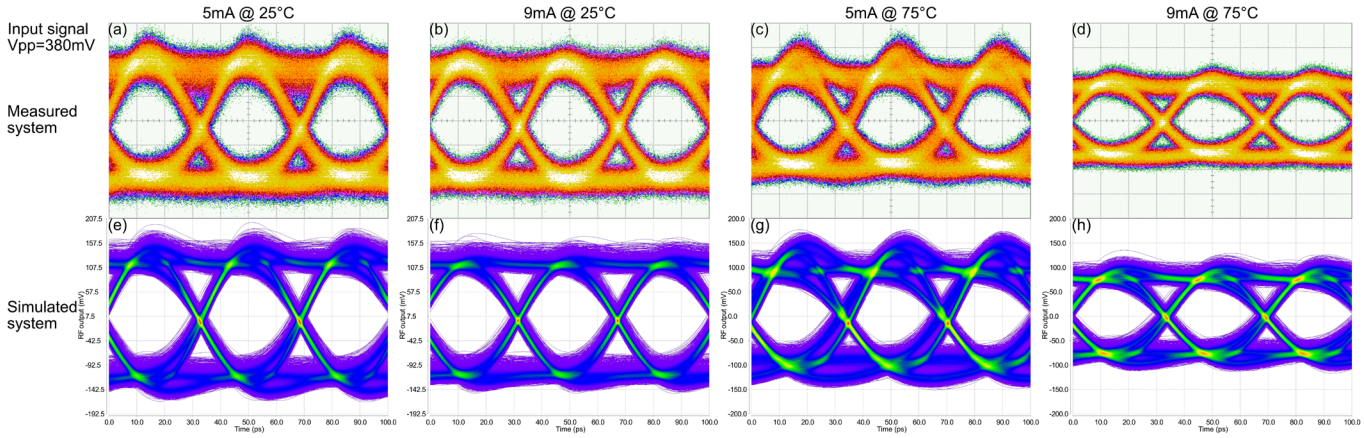

Fig. 6. Measured (a)-(d) and simulated (e) to (h) eye diagrams at 28 Gbaud OOK PRBS 15 modulation for the full back-to-back link set-up (i.e. driver, VCSEL, VOA, PD and microwave amplifier), employing the 28-GHz bandwidth VCSEL and in the simulations including all noise sources in the equivalent circuits for the VCSEL, PD, and AC-coupled amplifier. The peak-to-peak driver signal amplitude is 380 mV, and the VCSEL bias current and temperature is in (a) and (e) 5 mA and 25°C, (b) and (f) 9 mA and 25°C, (c) and (g) 5 mA and 75°C, and (d) and (h) 9 mA and 75°C. The eye diagrams are presented in density function mode. and the time and voltage scales, divisions and offsets for the simulated eye diagrams are set to be the same as for the corresponding measured eye diagrams for fairest comparison.

directly proportional to the DC-photocurrent generated in the PD. Note that as the noise is to be generated in the time domain it was found easier to use Verilog-A to generate these noise sources (just as for our VCSEL equivalent circuit), meaning that the PD equivalent circuit was partly implemented in Verilog-A. Thirdly, an AC-coupled microwave amplifier added with a time domain noise source (also implemented in Verilog-A for simplicity) and a 12-order Butterworth low-pass filter, to give the same noise figure and bandwidth-limited modulation response as specified by the manufacturer.

Fig. 5 shows examples of simulated eye diagrams generated from the VCSEL output, i.e. the simulated signal just before the VOA and PD equivalent circuits. A temporal resolution of 1 ps or better was applied in the simulations. The eye diagrams are for 28 Gbaud OOK modulation at 5 mA VCSEL bias current and at an ambient temperature of 25°C, and serve to illustrate the penalty in eye closure of using PRBS 15 instead of PRBS 7, and likewise for including or not including VCSEL intensity noise in the simulations. Comparing Fig. 5 (a) and (c), i.e. PRBS 7 versus PRBS 15 performance with noise sources disabled, a PRBS-penalty is clearly observed, which stems from the more lower frequencies excited in the PRBS 15 signal, due to a larger number of consecutive "0" or "1" bits. While this eye closure penalty in using PRBS 15 instead of 7 is not insignificant at this bit rate (also experimentally confirmed in [15]), the eye closure from including VCSEL intensity noise is stronger. This is seen by comparing Fig. 5 (a) with (b) and (c) with (d), where the noise sources are enabled in (b) and (d). This demonstrates how important it is to include VCSEL intensity noise in a large-signal datacom VCSEL equivalent circuit model.

Fig. 6 and Fig. 7 present a comparison of measured and simulated eye diagrams for the full back-to-back link, operating

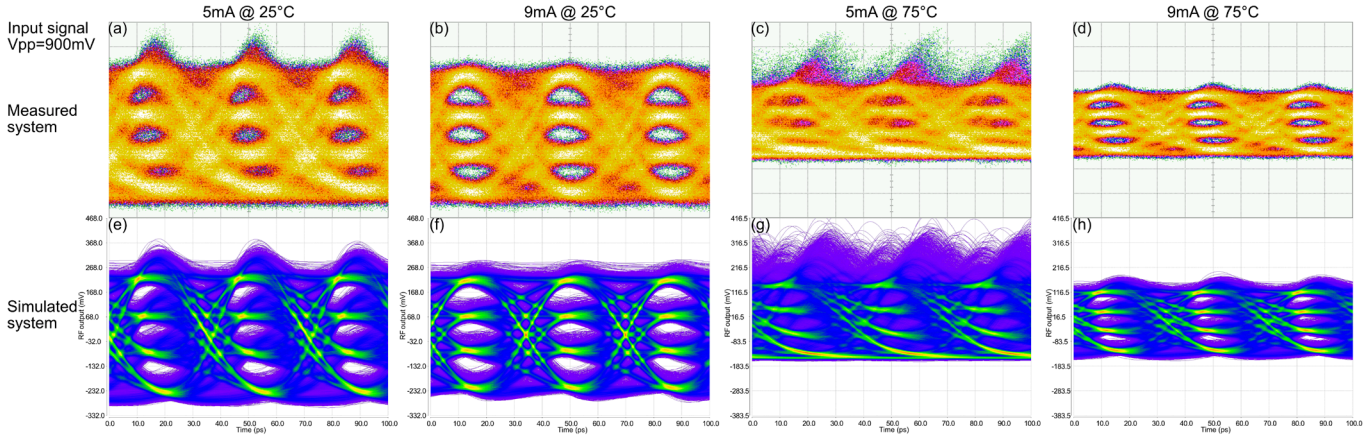

Fig. 7. Measured (a)-(d) and simulated (e) to (h) eye diagrams at 28 Gbaud PAM4 PRBS 15 modulation for the full back-to-back link set-up (i.e. driver, VCSEL, VOA, PD and microwave amplifier), employing the 28-GHz bandwidth VCSEL and in the simulations including all noise sources in the equivalent circuits for the VCSEL, PD, and AC-coupled amplifier. The driver peak-to-peak signal amplitude is 900 mV, and the VCSEL bias current and temperature is in (a) and (e) 5 mA and 25°C, (b) and (f) 9 mA and 25°C, (c) and (g) 5 mA and 75°C, and (d) and (h) 9 mA and 75°C. The eye diagrams are presented in density function mode. and the time and voltage scales, divisions and offsets for the simulated eye diagrams are set to be the same as for the corresponding measured eye diagrams for fairest comparison.

at 28 Gbaud OOK PRBS 15 respective PAM4 PRBS 15 modulation. Eye diagrams are shown for VCSEL ambient temperatures of 25°C and 75°C, both for VCSEL bias currents of 5 mA and 9 mA, which were used in [3] when generating the corresponding noise-free eye diagrams. Note that the threshold current is 0.7 mA and 0.9 mA, and the thermal roll-over current is 13.0 mA and 9.5 mA at 25°C and 75°C, respectively [3]. For all OOK cases the peak-to-peak modulation voltage is 380 mV, while for all PAM4 cases the peak-to-peak modulation voltage is 900 mV. In the simulations a temporal resolution of 1 ps or better was applied. For providing as fair as possible comparison between measured and corresponding simulated eye-diagrams, the same time and voltage scales, divisions and offsets are applied. The link eye diagram simulations show nice agreement with the corresponding measured eye diagrams, in predicting both the eye waveform and eye closure from bit-pattern history and noise effects, and this for a wide range of driving conditions for the link.

IV. Conclusion

A large-signal equivalent circuit model for high-speed datacom VCSELs is presented. It is based on the same equivalent circuit model as presented by the authors earlier in [3], that is able to accurately reproduce the large-signal modulation waveform response of a state-of-the-art 28-GHz bandwidth 850-nm VCSEL for a broad range of driving conditions, e.g. bias current, modulation voltage, ambient temperature, and modulation format. This datacom VCSEL equivalent circuit model is here extended so that it can also accurately predict the intensity noise properties in the output from the same VCSEL.

The VCSEL equivalent circuit model consists of five interdependent sub-circuits, treating the device input impedance, carrier accumulation in the SCH, carrier accumulation in the QWs, number of photons in the resonator, and device self-heating, respectively. Thermal noise is introduced for the distributed electrical resistances in sub-circuit 1, and shot noise following Poisson statistics is introduced in sub-circuit 2-4 for almost all individual physical processes considered. The feedback mechanism in the generation of photons and the accumulation of carriers in the QWs from the stimulated recombination process is responsible for that the intensity noise in the output from the VCSEL is not pure shot noise, i.e. white noise, but is colored noise with a peak at the resonance frequency.

To verify our noise implementation, our noise extended VCSEL equivalent circuit model is applied for the same 28-GHz-bandwidth 850-nm VCSEL as in [3] and simulated RIN spectra are compared to measured RIN spectra. Thereafter, large-signal eye diagrams for a simple back-to-back 28 Gbaud PRBS 15 OOK and PAM4 link set-up, applying the same VCSEL, is simulated and compared to measurements. Good agreement in RIN spectrum and eye diagrams are found, for a wide range of bias currents, modulation voltages, and ambient temperatures that are typically for datacom applications.

The purpose of the work is primarily to provide a VCSEL equivalent circuit model to datacom link designers that is able to accurately mimic not only the waveform but also the noise in the optical output from a datacom VCSEL under high-speed large-signal modulation. Secondarily, to have such a model that can also to a high degree link the VCSEL bandwidth and noise performance limitations to the VCSEL design. This by making it as physics-based as possible. This kind of datacom VCSEL equivalent circuit model will be needed in the design of future OIs, requiring the co-design and optimization of driver electronics, VCSEL, and receiver electronics.

Potential future work will consist of expanding the temperature range in which our datacom VCSEL equivalent circuit model has proven to work well. This to not only accommodate conventional OI applications, but also novel link applications operating at lower and higher temperatures. For example, sub-zero to >100°C temperatures demanded by the automotive industry [16], and temperatures at or higher than 100°C for transceivers that are placed on the same ASIC boards as used for data processing [17] e.g. in applications such as high-performance computing.

Acknowledgment

The authors would like to thank Dr. Stavros Giannakopoulos at Chalmers University of Technology for aid in Cadance circuit simulations, Dr. Richard Schatz at Royal Institute of Technology, Stockholm, Sweden, for theoretical advice, and Dr. Attila Fülöp at Nvidia Corporation, Gothenburg, Sweden, for datacom VCSEL parameters. This project was financially supported by the Swedish Foundation for Strategic Research (CHI19-0004).

References

[1] D. Mahgerefteh and C. Thompson, "Techno-economic Comparison of Silicon Photonics and Multimode VCSELs," in *Optical Fiber Communication Conference*, 2015, vol. 34, no. 2, p. M3B.2. doi: 10.1364/OFC.2015.M3B.2.

[2] T. Lengyel, K. Szczerba, E. P. Haglund, P. Westbergh, M. Karlsson, A. Larsson, and P. A. Andrekson, "Impact of Damping on 50 Gbps 4-PAM Modulation of 25G Class VCSELs," *J. Light. Technol.*, vol. 35, no. 19, pp. 4203–4209, Oct. 2017, doi: 10.1109/JLT.2017.2727549.

[3] A. Grabowski, J. Gustavsson, Z. S. He, and A. Larsson, "Large-Signal Equivalent Circuit for Datacom VCSELs," *J. Light. Technol.*, vol. 39, no. 10, pp. 3225–3236, May 2021, doi: 10.1109/JLT.2021.3064465.

[4] A. Melgar, V. A. Thomas, B. D. B. Klein, I. Kalifa, P. Bakopoulos, E. Mentovich, and S. E. Ralph, "Behavioral PAM-4 VCSEL Model using Stochastic Multimode Rate Equations for Link Design Optimization," in *2022 Optical Fiber Communications Conference and Exhibition (OFC)*, 2022, pp. 1–3.

[5] S. Li, M. S. Nezami, D. Rolston, and O. Liboiron-Ladouceur, "A Compact High-Efficient Equivalent Circuit Model of Multi-Quantum-Well Vertical-Cavity Surface-Emitting Lasers for High-Speed Interconnects," *Appl. Sci.*, vol. 10, no. 11, p. 3865, Jun. 2020, doi: 10.3390/app10113865.

[6] J. S. Gustavsson, J. Bengtsson, and A. Larsson, "Spatially dependent noise model for vertical-cavity surface-emitting lasers," *IEEE J. Quantum Electron.*, vol. 40, no. 9, pp. 1163–1176, Sep. 2004, doi: 10.1109/JQE.2004.833211.

[7] S. Voinigescu, *High-Frequency Integrated Circuits*. Cambridge: Cambridge University Press, 2013.

[8] G. P. Agrawal, *Fiber-Optic Communication Systems*. Wiley, 2010.

[9] L. A. Coldren, S. W. Corzine, and M. L. Mašanović, *Diode Lasers and Photonic Integrated Circuits*, 2nd ed., vol. 218. Hoboken, NJ, USA: John Wiley & Sons, Inc., 2012.

[10] Y. Yamamoto, *Coherence, amplification and quantum effects in semiconductor lasers.* Wiley, 1991.

[11] R. C. Hilborn, "Einstein coefficients, cross sections, f values, dipole moments, and all that," *Am. J. Phys.*, vol. 50, no. 11, pp. 982–986, Nov. 1982, doi: 10.1119/1.12937.

[12] P. Westbergh, R. Safaisini, E. Haglund, J. S. Gustavsson, A. Larsson, and A. Joel, "High-speed 850 nm VCSELs with 28 GHz modulation

bandwidth for short reach communication," in *Proc. SPIE, Vertical-Cavity Surface-Emitting Lasers XVII*, Mar. 2013, vol. 8639, pp. 86390X-1–6. doi: 10.1117/12.2001497.

[13] A. Larsson, "Advances in VCSELs for Communication and Sensing," *IEEE J. Sel. Top. Quantum Electron.*, vol. 17, no. 6, pp. 1552–1567, Nov. 2011, doi: 10.1109/JSTQE.2011.2119469.

[14] J. Y. Law and G. P. Agrawal, "Mode-partition noise in vertical-cavity surface-emitting lasers," *IEEE Photonics Technol. Lett.*, vol. 9, no. 4, pp. 437–439, Apr. 1997, doi: 10.1109/68.559380.

[15] A. Larsson, E. Simpanen, J. S. Gustavsson, E. Haglund, E. P. Haglund, T. Lengyel, P. A. Andrekson, W. V. Sorin, S. Mathai, M. Tan, and S. R. Bickham, "1060 nm VCSELs for long-reach optical interconnects," *Opt. Fiber Technol.*, vol. 44, no. November 2017, pp. 36–42, Aug. 2018, doi: 10.1016/j.yofte.2018.01.001.

[16] A. Rodríguez-Pérez, R. Pérez de Aranda, E. Prefasi, S. Dumont, J. Rosado, I. Enrique, P. Pinzón, and D. Ortiz, "Toward the Multi-Gigabit Ethernet for the Automotive Industry," *Fiber Integr. Opt.*, vol. 40, no. 1, pp. 1–13, Jan. 2021, doi: 10.1080/01468030.2021.1916695.

[17] C. Kuznia and C. Tabbert, "Chip scale package fiber optic transceiver integration for harsh environments," in *International Conference on Space Optics — ICSO 2014*, Nov. 2017, vol. 10563, no. October 2014, p. 114. doi: 10.1117/12.2304174.

Alexander Grabowski received the M.Sc. degree in electrical engineering from Chalmers University of Technology, Göteborg, Sweden, in 2017. The same year, he joined the Department of Microtechnology and Nanoscience at Chalmers, where he is currently working toward the Ph.D. degree working on GaAs-based vertical-cavity surface-emitting lasers (VCSELs) in high-speed short-reach optical interconnects, mainly focusing on modelling of the VCSEL. He has also done work on fabrication of GaAs-based VCSELs for micro-transfer-printing integration on a silicon nitride PIC platform.

Johan S. Gustavsson received his M.Sc. degree in Electrical Engineering and his Ph.D. degree in Photonics from Chalmers University of Technology, Göteborg, Sweden, in 1998 and 2003, respectively. His Ph.D. thesis was focused on mode dynamics and noise in vertical-cavity surface-emitting lasers (VCSELs).

Since 2003 he has been a researcher at the Photonics Laboratory, at Chalmers, with an Assistant Professor position 2004-2008, and an Associate Professor position from 2011. In Sept.-Oct. 2009 he was a visiting scientist at CNR Polytechnico, Turin, Italy, and in 2017 he co-organized the European Semiconductor Laser Workshop in Copenhagen. In 2016, he co-founded the spin-off company OptiGOT AB, which was in 2020 acquired by Nvidia Corp. He has authored or coauthored more than 250 scientific journal and conference papers and two book chapters, and his research has been focused on semiconductor lasers for short to medium reach communication, and sensing applications. This has included surface relief techniques for mode and polarization control in VCSELs, 1.3 µm InGaAs VCSELs/GaInNAs ridge waveguide lasers for access networks, 2.3-3.5 µm GaSb VCSELs for CO, CO_2 and NH_3 sensing, and tunable VCSELs via moveable mirror for reconfigurable optical interconnects. He is currently working on energy efficient 56 Gbaud GaAs-based VCSELs for next generation datacom links, UV/blue AlGaN/GaN VCSELs for sterilizing/illumination, high contrast gratings as feedback/wavelength setting/focusing elements in micro-cavity lasers, and heterogeneous integration of III/V-based VCSEL material on a Si-platform. He is also exploring photon-photon resonance effects to boost the modulation bandwidth in GaAs-based VCSELs.

Anders Larsson received the M.Sc. and Ph.D. degrees in electrical engineering from Chalmers University of Technology, Göteborg, Sweden, in 1982 and 1987, respectively. In 1991, he joined the faculty at Chalmers where he was promoted to Professor in 1994. From 1984 to 1985, he was with the Department of Applied Physics, California Institute of Technology, and from 1988 to 1991 with the Jet Propulsion Laboratory, both at Pasadena, CA, USA. He has been a guest professor at Ulm University (Germany), at the Optical Science Center, University of Arizona at Tucson (USA), at Osaka University (Japan), and at the Institute of Semiconductors, Chinese Academy of Sciences (China). He co-organized the IEEE Semiconductor Laser Workshop 2004, organized the European Semiconductor Laser Workshop 2004, was a co-program chair for the European Conference on Optical Communication 2004, and was the program and general chair for the IEEE International Semiconductor Laser Conference in 2006 and 2008, respectively. He was a member of the IEEE Photonics Society Board of Governors (2014-2016), an associate editor for IEEE/OSA Journal of Lightwave Technology (2011-2016) and a member of the editorial board of IET Optoelectronics (2007-2020). In 2016, he co-founded OptiGOT AB, which was acquired by Nvidia in 2020. His scientific background is in the areas of optoelectronic materials and devices for optical communication, information processing, and sensing. Currently, his research is focused on vertical-cavity surface-emitting lasers and optical interconnects. He has published close to 600 scientific journal and conference papers and 2 book chapters. He is a Fellow of IEEE, OSA, and EOS. In 2012, he received the HP Labs Research Innovation Award.